Letter Vol. 47, No. 23 / 1 December 2022 / Optics Letters 6081

Optical phased array with on-chip phase calibration

Mathias Prost, Jon Øyvind Kjellman, Sarvagya Dwivedi, Aleksandrs Marinins, Hemant Kumar Tyagi, Tangla David Kongnyuy, Philippe Soussan, Marcus S. Dahlem, Xavier Rottenberg, and Roelof Jansen*

Interuniversity Microelectronics Center (IMEC), Kapeldreef 75, 3001 Leuven, Belgium
**Corresponding author: roelof.jansen@imec.be*

Received 12 July 2022; revised 16 September 2022; accepted 16 September 2022; posted 19 September 2022; published 16 November 2022

Optical phased arrays (OPAs) with phase-monitoring and phase-control capabilities are necessary for robust and accurate beamforming applications. This paper demonstrates an on-chip integrated phase calibration system where compact phase interrogator structures and readout photodiodes are implemented within the OPA architecture. This enables phase-error correction for high-fidelity beam-steering with linear complexity calibration. A 32-channel OPA with 2.5-μm pitch is fabricated in an Si–SiN photonic stack. The readout is done with silicon photon-assisted tunneling detectors (PATDs) for sub-bandgap light detection with no-process change. After the model-based calibration procedure, the beam emitted by the OPA exhibits a sidelobe suppression ratio (SLSR) of −11 dB and a beam divergence of 0.97° × 0.58° at 1.55-μm input wavelength. Wavelength-dependent calibration and tuning are also performed, allowing full 2D beam steering and arbitrary pattern generation with a low complexity algorithm. © 2022 Optica Publishing Group

https://doi.org/10.1364/OL.467779

The development of optical phased array (OPA) devices based on photonic integrated circuits (PICs) has seen a significant growth driven by emerging applications such as free-space optical communications (FSOC) and light detection and ranging (lidar) [1]. Silicon photonics allows dense integration using fabrication processes from CMOS foundries. Since the early demonstration of an OPA on a silicon-photonic platform [2], the number of channels has scaled up to thousands in recent demonstrations [3]. The beam quality generated by OPAs improves with increasing aperture size and the number of elements. However, inherent fabrication errors affect the performance of large-scale photonic devices [4,5]. Small variations of the waveguide properties such as width, thickness, material density, or roughness can lead to phase-error accumulation for identical path routing in mm-scale circuits. This is especially detrimental in OPA devices, where all channels need to be in phase to operate properly. For example, devices fabricated with silicon waveguide feeding networks cannot be operated without phase error calibration. The typical approach to calibrate an OPA is to measure the emitted beam at the desired angle position in the far-field and maximize a figure of merit using hill-climbing, particle swarm optimization, or gradient descent algorithms [6–8]. A dedicated optical setup is needed to achieve the calibration, which would increase the difficulty of performing re-calibration if the device is integrated into a larger system. On-chip calibration approaches have been proposed based on diffraction pattern imaging at the end of the output emitting array, but these approaches still rely on an algorithm that maximizes a figure of merit from the generated optical signal [9,10].

In our previous work [11], we demonstrated a different approach using phase interrogators (PIs) that can be tightly integrated with the OPA architecture right before the emitting aperture stage. The PI is a photonic structure that allows retrieval of the phase error between two waveguides. A fraction of the optical signal of each waveguide is combined to create an interferometric signal that depends on the phase difference. By monitoring this interferometric signal, the phase error of every waveguide in the array can be extracted using a physical model and a simple fit procedure. As an initial proof-of-concept, the phase-interrogator interferometric signals were monitored by external optical readouts in our previous devices [12]. In this paper, we present the results of a calibrated OPA using photodiode (PD) arrays for the signal readout, making this a truly on-chip solution. The PD arrays rely on photon-assisted tunneling PDs (PATDs) where the silicon waveguide has an implanted *p-n* junction and can detect a sub-bandgap wavelength under a reverse bias [13,14]. This type of device has the advantages of no-process change of the silicon photonics platform and no additional growth of germanium, while offering sufficient performance for calibration purposes. With this approach of using on-chip phase-interrogators, the phase calibration only requires low computational complexity, and can theoretically be executed for live recalibration of the chip.

The OPA architecture is based on a uniform linear array (ULA), as depicted in Fig. 1(b). It is implemented in a 200-mm deep ultraviolet SiN/Si process stack [15]. The optical routing part is achieved using an SiN waveguide photonics layer to ensure low loss propagation and low phase error [5]. The phase shifter stage, phase interrogators, and the emitting aperture are fabricated in the Si layer for efficient and compact optical circuits. The aperture consists of an array of leaky-wave antennas (LWAs) formed by weak grating emitters. The grating emitters are made of SiN scatterer boxes placed on top of the Si waveguides [12]. It ensures low strength out-of-plane coupling to form half-mm-long emitters. The LWA array pitch is 2.5 μm. This pitch allows low optical cross talk while leaving sufficient

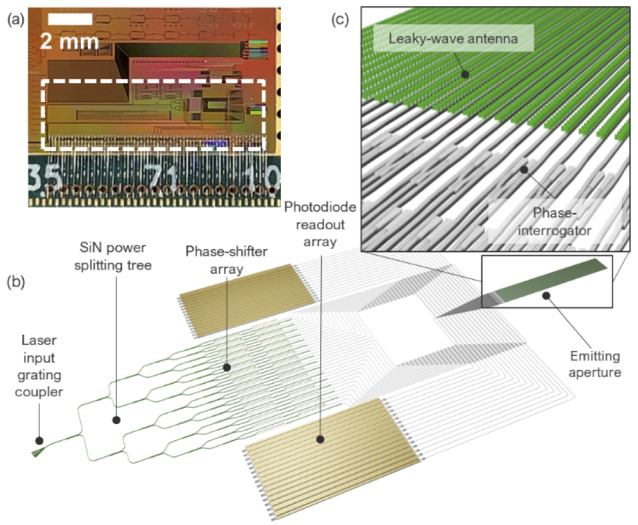

Fig. 1. Details of the OPA: (a) picture of the packaged die where the OPA circuit is boxed with the white dotted line; (b) schematic representation of the 32-channel OPA circuit with integrated photodiodes for on-chip beam-steering calibration; (c) zoomed-in view of the compact phase interrogators placed before the emitting aperture.

space to fit the phase interrogator in between two waveguides. The design of the phase interrogator device is shown in Fig. 1(c) and it is thoroughly described in [12]. Based on these dimensions, the ambiguous steering range is $\pm 19.2°$ at $\lambda = 1.55\ \mu m$ [16]. The OPA uses silicon thermo-optic phase shifters with top tungsten heaters. These thermal phase-shifters have a measured efficiency of 30 mW/π. The fabricated device is shown in Fig. 1(a). For the calibration readout, the PATD devices have a 1-mm-long active section. The characteristics of the sub-bandgap photodetectors are discussed in [14].

The principle of the phase calibration procedure is described in the schematic shown in Fig. 2(a). Considering a given waveguide i of the array, the phase ϕ_i before the emitting aperture is defined by the accumulated phase $\phi_{err,i}$ and by an induced phase change by the phase shifter which is dependent on the applied electrical power P_i and the thermo-optic proportionality constant k_i as

$$\phi_i = \phi_{err,i} + k_i P_i. \tag{1}$$

When using a voltage source V_i to drive the phase shifter, the applied electrical power can be decomposed using the electrical resistance $R(V_i)$ of the heating element into the following expression:

$$P_i = R(V_i) \times V_i^2 = [R_{0,i} + \alpha_{R,i} V_i^2], \tag{2}$$

where $R_{0,i}$ and $\alpha_{R,i}$ are the parameters to model the nonlinear behavior of the resistance due to self-heating. To extract the phase difference $\Delta\phi_i$ between two neighboring waveguides, a fraction of the optical signals of the waveguides i and $i+1$ are combined to create an optical interferometric signal$I_{PI,i}$ by the phase-interrogator. This signal is dependent of the phase difference $\Delta\phi_i$ between the two monitored waveguides, described by the following equation:

$$I_{PI,i}(V_i,\ V_{i-1}) = A_i + B_i cos(\Delta\phi_i(V_i,\ V_{i-1})). \tag{3}$$

From this signal, it is possible to calculate the induced phase shift required to cancel the phase error difference. The parameters of the thermal phase-shifters $\{k_i,\ R_{0,i},\ \alpha_{R0,i}\}$ are fully extracted,

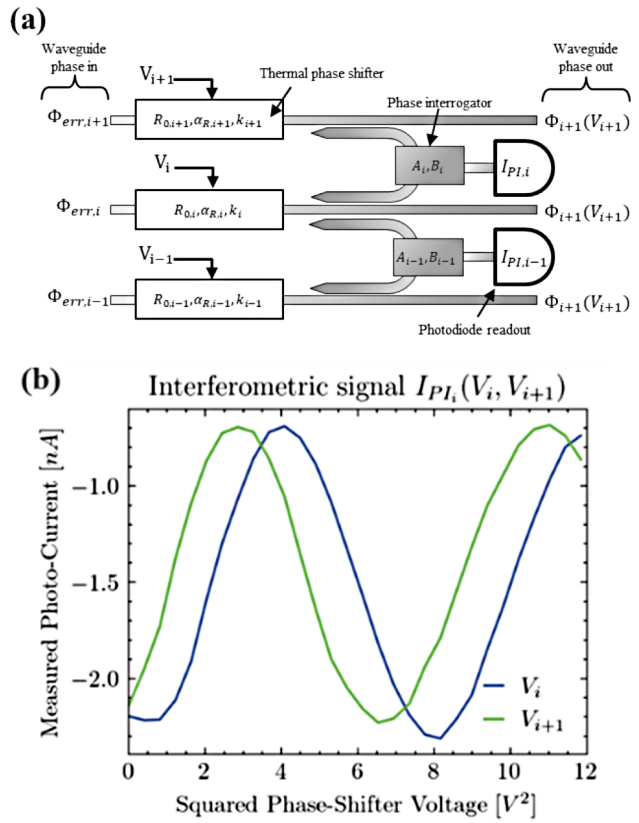

Fig. 2. Principle of phase calibration: (a) diagram of the phase interrogator architecture implemented in the OPA showing the different components and parameters used to extract the phase error; (b) example of measured $I_{PI,i}$ current signal with a PATD while sweeping the applied voltage of the thermal phase-shifters V_i and V_{i+1}.

thereby an arbitrary linear phase shift can be computed to enable beam-steering or pattern generation.

The look-up table (LUT) used to obtain calibrated beam-steering is populated by extracting the $\{\Delta\phi_{err,i},\ k_i,\ R_{0,i},\ \alpha_{R,i}\}$ parameters. The procedure is achieved in two steps. In the first step, the current–voltage behavior of each thermal phase-shifter is measured to determine the nonlinear dependence of the resistor due to the self-heating effect, with the parameters $R_{0,i}$ and $\alpha_{R,i}$. In the second step, the response of the phase interrogator $I_{PI,i}$ is measured by reading-out the current signal of the PATD. The photocurrent is acquired by a source measurement unit (SMU, Keithley 2400) in combination with an electronic switch to address the different PATDs of the array. The diode is operated under a reverse bias of 1 V in the low-gain regime but with lower dark current. The phase-shifters are driven by a custom multi-channel voltage driver. The voltages V_i and V_{i+1} applied on the phase-shifter pair associated with a PI is swept sequentially. The change of the photocurrent due to the modulation of the interferometric optical signal $I_{PI,i}$ by the applied voltage is recorded, as shown in Fig. 2(b). Once the data for all the channels of the array are acquired, we fit the data to a model to extract the phase error $\phi_{err,i}$ and the characteristics of the phase shifter k_i based on Eqs. (1) and (3). The built LUT can generate the voltages $\{V_{n,\psi_s}\}$ needed for the phase-shifter array to cancel $\phi_{err,i}$ and get a calibrated beam spot at the desired steering angle ψ_s. The algorithm is fitting the multiple datasets simultaneously because the parameter for the phase shifter k_i is dependent within

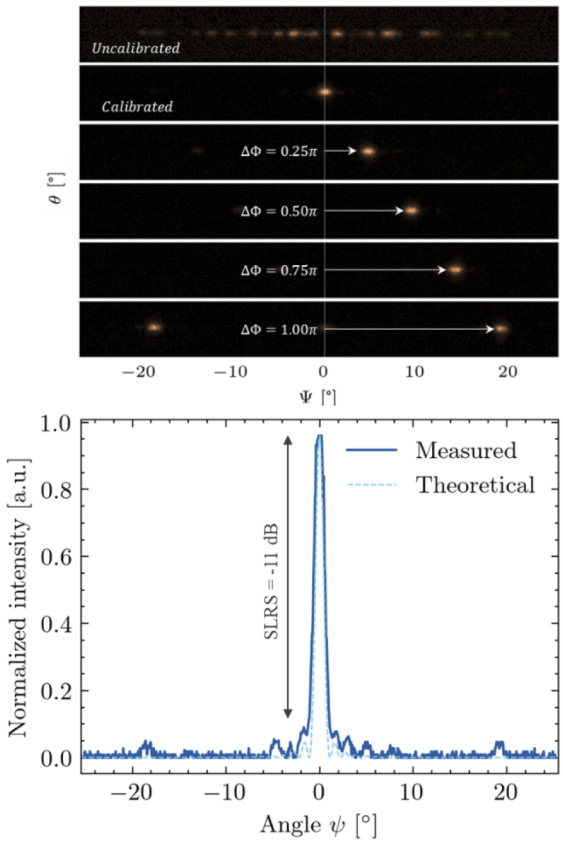

Fig. 3. (a) Captured back focal plane image of the emitted beam before calibration, after calibration for a 32-element OPA at $\lambda = 1550$ nm, and for a set of applied linear phase shifts $\Delta\Phi$ from 0 to π by $\pi/4$ steps. (b) Calibrated beam image cutline along the ψ direction showing the normalized measured and theoretical beam profile.

two PIs' response signals. The calibration speed of the system is mainly limited by the sequential interface acquisition of the photocurrent signal which takes approximately 20 s per phase-shifter sweep. The calibration time can be strongly reduced by using a dedicated digital–analog interface with parallel acquisition of the PI response of every second pair. With sufficient parallel computing resources, live calibration of the system can be enabled, as for a single calibration loop, and all the steerable angles ψ_s can be generated from the LUT.

After the calibration procedure, the emitting beam properties of the OPA are characterized using a back-focal plane setup. The beam is captured with a 20× magnification microscope objective and a numerical aperture of 0.40, and then projected on an infrared camera with a $2f$ lens system. Figure 3(a) shows the captured beam before and after the calibration. After applying the voltage set $\{V_{n,\psi_s=0}\}$ calculated from the LUT, the beam quality is significantly improved from a random pattern to a well-defined beam-spot as the phase errors due to light propagation are corrected. The input laser wavelength is 1550 nm. For a 32-channel OPA with a 0.48-mm-long aperture, the theoretical full width at half maximum (FWHM) beam divergence is $0.98° \times 0.29°$. We measured an FWHM of $0.97° \times 0.58°$ for the $\delta\Psi$ and $\delta\theta$ axes, respectively. The measured value $\delta\psi$ is in good agreement with the theoretical one, while the $\delta\theta$ is larger than the predicted one. The LWA design is based on SiN grating scatterers where fill-factor variation and thickness variation along the LWA length can occur and give an error on the emitting angle, leading to broader beam divergence. Figure 3(b) shows a cutline in the transversal direction along the ψ axis. Since the camera used to capture the far-field has a limited dynamic range, we applied the method proposed by [17] to determine accurately the sidelobe suppression ratio (SLSR). The optical input power of the laser is increased until the signal intensity of the sidelobe reaches that of the mainlobe before the saturation. Thus, the optical power difference between those two input levels determines the SLSR. At $\lambda = 1550$ nm, we estimated the SLSR to be −11 dB, showing a good fidelity beam (−13.3 dB theoretical for the uniform linear array). The small error can be explained by residual phase errors not completely corrected. We also experienced some voltage drop on the phase shifters due to variation of the resistance in the common ground path. This leads to a small difference from the operating voltage set point of the phase shifters. This issue can be solved by controlling the phase shifters with current driving, or by improving the design of the ground connection of the heaters. Figure 3(a) shows beam steering by phase control along the transverse axis ψ by applying a linear phase shift $\Delta\phi$ between each channel of the OPA. Any beam position in the unambiguous steering range can be generated using the single calibration LUT and updating the phase shifters voltage array $\{V_{n,\psi_s}\}$.

Full 2D beam steering is achieved with wavelength tuning. In that case, the calibration procedure is repeated in steps of 10 nm for wavelengths between 1500 nm and 1560 nm. Above 1560 nm, the responsivity of the PDs starts to decrease. However, the phase errors have a linear dependency with the wavelength, and the LUT can be populated for longer wavelengths by linear extrapolation of the k_i and $\phi_{err,i}$ parameters, as shown in Figs. 4(a) and 4(b). By a combination of laser wavelength tuning from 1520 nm to 1580 nm and applying a linear phase shift generated by the LUT, we were able to produce a logo in a composite image,

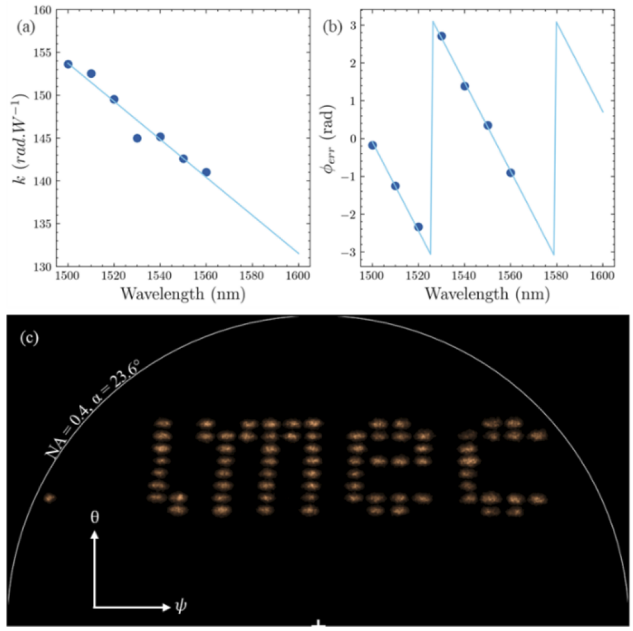

Fig. 4. Full 2D beam steering: (a) and (b) linear wavelength dependence of the calibration parameters k_i and $\phi_{err,i}$, respectively, obtained by one of the PIs; (c) composite image of the 2D beam steering obtained by a combination of laser wavelength tuning from 1520 nm to 1580 nm and applied linear phase shift. The solid white circle indicates the maximum measurable angle of the setup.

as shown in Fig. 4(c). The beams are generated on a rectangular grid, with setpoints calculated from the multi-wavelength LUT, and subsequently captured by the imaging system.

We demonstrated a 32-channel OPA with on-chip calibration using phase interrogators and sub-bandgap photon-assisted tunneling diodes operating near 1550 nm. The OPA is based on a dual layer SiN/Si photonics stack with silicon-only photodiodes for calibration readout. The calibrated beam spot exhibits a FWHM beam divergence of $0.97° \times 0.58°$ with a sidelobe suppression ratio of -11 dB. Full 2D beam-steering is achieved by the combination of wavelength tuning using few calibration points over the wavelength sweeping range. The calibration is shown to be valid for wavelengths beyond the sensitivity of the PDs. As the properties of the phase shifters are completely extracted during the calibration procedure, the algorithm enables random-access steering and pattern generation based on the LUT calculation with low-computation power. Phase calibration in OPAs is critical to ensure accurate operation, and this paper shows an attractive method to achieve on-chip calibration and continuous monitoring of the phase errors. The proposed approach relies on a simple model that allows fast calibration and leverages the need for an external setup to perform the optimization of the emitted beam. This OPA architecture with on-demand on-chip calibration can be used to achieve reliable performance levels in PICs designed for applications such as FSOC or lidar.

Disclosures. The authors declare no conflicts of interest.

Data availability. Data underlying the results presented in this paper are not publicly available at this time but may be obtained from the authors upon reasonable request.

REFERENCES

1. M. J. R. Heck, Nanophotonics **6**, 93 (2017).
2. K. V. Acoleyen, W. Bogaerts, J. Jágerská, N. L. Thomas, R. Houdré, and R. Baets, Opt. Lett. **34**, 1477 (2009).
3. C. V. Poulton, M. J. Byrd, B. Moss, E. Timurdogan, R. Millman, and M. R. Watts, in *2020 Conference on Lasers and Electro-Optics (CLEO)* (2020), pp. 1–2.
4. W. Bogaerts and L. Chrostowski, Laser Photonics Rev. **12**, 1700237 (2018).
5. S. Dwivedi, H. K. Tyagi, A. Marinins, S. Kerman, T. D. Kongnyuy, J. Ø. Kjellman, B. Figeys, M. Prost, S. Saseendran, P. Soussan, M. S. Dahlem, X. Rottenberg, and R. Jansen, in *OSA Advanced Photonics Congress (AP) 2019 (IPR, Networks, NOMA, SPPCom, PVLED)* (Optical Society of America, 2019), p. IM4A.3.
6. J. K. Doylend, M. J. R. Heck, J. T. Bovington, J. D. Peters, L. A. Coldren, and J. E. Bowers, Opt. Express **19**, 21595 (2011).
7. S. Chung, H. Abediasl, and H. Hashemi, IEEE J. Solid-State Circuits **53**, 275 (2018).
8. T. Kim, P. Bhargava, C. V. Poulton, J. Notaros, A. Yaacobi, E. Timurdogan, C. Baiocco, N. Fahrenkopf, S. Kruger, T. Ngai, Y. Timalsina, M. R. Watts, and V. Stojanović, IEEE J. Solid-State Circuits **54**, 3061 (2019).
9. T. Komljenovic and P. Pintus, Opt. Express **26**, 3199 (2018).
10. J. Shim, J.-B. You, H.-W. Rhee, H. Yoon, S.-H. Kim, K. Yu, and H.-H. Park, Opt. Lett. **45**, 6058 (2020).
11. J. Ø. Kjellman, M. Prost, A. Marinins, H. K. Tyagi, T. D. Kongnyuy, S. Kerman, B. Troia, B. Figeys, S. Dwivedi, M. S. Dahlem, P. Soussan, X. Rottenberg, and R. Jansen, in *Integrated Optics: Devices, Materials, and Technologies XXIV*, S. M. García-Blanco and P. Cheben, eds. (SPIE, 2020), Vol. 11283, pp. 98–104.
12. J. Ø. Kjellman, M. Prost, A. Marinins, H. K. Tyagi, T. D. Kongnyuy, S. Dwivedi, M. S. Dahlem, P. Soussan, X. Rottenberg, and R. Jansen, J. Lightwave Technol. **40**, 5660 (2022).
13. J.-B. You, H. Kwon, J. Kim, H.-H. Park, and K. Yu, Opt. Express **25**, 4284 (2017).
14. S. Dwivedi, J. Kjellman, T. David, M. Prost, O. Syshchyk, E. Van Sieleghem, J. Lee, A. Marinins, P. Soussan, M. Dahlem, X. Rottenberg, and R. Jansen, IEEE Photonics Technol. Lett. **33**, 836 (2021).
15. A. Marinins, S. P. Dwivedi, JØ Kjellman, S. Kerman, K. Tangla, B. Figeys, R. Jansen, D. S. Tezcan, X. Rottenberg, and P. Soussan, Jpn. J. Appl. Phys. **59**, SGGE02 (2020).
16. C. A. Balanis, *Antenna Theory: Analysis and Design, 4th Edition* (Wiley-Interscience, 2016).
17. D. N. Hutchison, J. Sun, J. K. Doylend, R. Kumar, J. Heck, W. Kim, C. T. Phare, A. Feshali, and H. Rong, Optica **3**, 887 (2016).

146.103.254.11 on 2023-04-06 09:47 UTC